JOURNAL OF PROPULSION AND POWER
Vol. 11, No. 4, July–August 1995

Numerical Simulations of Injection-Driven Flows in a Two-Dimensional Nozzleless Solid-Rocket Motor

Tong-Miin Liou* and Wan-Yih Lien†
National Tsing Hua University, Hsinchu, Taiwan 300, Republic of China

A numerical analysis has been performed to study cold flows in a nozzleless solid-rocket motor (SRM) consisting of a two-dimensional porous-walled duct and an impermeable-walled diverging expansion section. The finite volume technique was used to solve the Navier–Stokes equations without subgrid-scale turbulence models, and the numerical fluxes were computed using a modified Godunov's scheme. Computed results are compared with existing experimental data, including mean pressure and axial velocity, the transition process of the mean-velocity profile, the level and shift of the turbulence intensity peak, and the pressure contour near the diverging expansion region. Furthermore, this study addresses the effects of wall injection on the near-wall velocity profiles of the fully turbulent flat-plate flow and the validity of the "law of the wall" throughout the flowfield in an SRM.

Nomenclature

B^+ = empirical constant
C_f = skin friction coefficient, $\tau_w/(\rho u^2/2)$
e = total energy per unit volume, J/m^3
$\boldsymbol{F}$ = convective flux vector in x direction of Navier–Stokes equations
$\boldsymbol{G}$ = convective flux vector in y direction of Navier–Stokes equations
h = duct half-height, m
I = turbulence intensity, $(\overline{u'^2} + \overline{v'^2})^{1/2}$, m/s
I_p = peak value of turbulence intensity, m/s
k = turbulence kinetic energy, m^2/s^2
k_{ab} = turbulence kinetic energy at wall in absence of any shear effects, m^2/s^2
L = duct length, m
p = pressure, N/m^2
$\boldsymbol{Q}$ = conservation variables vector of Navier–Stokes equations
Re_c = centerline axial Reynolds number, $\bar{u}_c h/\nu$
Re_w = injection Reynolds number, $\bar{v}_w h/\nu$
T = temperature, K
t = time coordinate, s
u = velocity in x direction, m/s
u^+ = u/u_τ
u_τ = $\sqrt{\tau_w/\rho}$, m/s
v = velocity in y direction, m/s
v_w = blowing or injection velocity, m/s
v_w^+ = v_w/u_τ
x, y = Cartesian coordinates
y^+ = yu_τ/ν
y_p = location of I_p from porous wall
β = momentum flux coefficient, $\int_0^{-2} dy/(\bar{u}_b^2 h)$
ε = dissipation rate of turbulence kinetic energy, m^2/s^3
ι = turbulence length scale, m
ι_{ab} = turbulence length scale at wall in absence of any shear effects, m
κ = thermal conductivity, W/(m·K)
λ = bulk viscosity, kg/(m·s)
μ = molecular viscosity, kg/(m·s)
ν = dynamic viscosity, m/s^2
ρ = density, kg/m^3
σ_s = surface-generated pseudoturbulence, $\sqrt{\overline{v'v'}}/\bar{v}_w$
τ = shear stress, N/m^2
ω = pseudovorticity, 1/s

Subscripts
b = bulk mean value, cross-sectionally averaged
c = centerline
h = head-end
w = wall

Superscripts
$'$ = turbulent fluctuating value of variables
$\bar{}$ = average value

Introduction

ENGINEERING applications such as boundary-layer control, transpiration cooling, and the combustion-induced flowfield in a solid-rocket motor (SRM) are related to the flowfield in a duct with fluid sucked or injected through porous walls. The flow in a solid-propellant rocket motor plays an important role in ballistics prediction, which is affected by the erosive burning behavior of the solid propellant. Erosive burning is related to the transverse shift of the turbulence intensity peak toward the burning surface[4] and is often present in nozzleless SRMs. This article is concerned with the flow characteristics in a nozzleless SRM.

Early attempts to investigate the internal flowfield of an SRM were mainly concerned with the distribution of the mean velocity. Using the inviscid Euler equation and laminar theory, Taylor[1] and Culick[2] derived similar velocity profiles for flows in a closed head-end channel subjected to the boundary condition of uniform wall injection as follows:

$$\bar{u}/\bar{u}_c = \sin[(\pi/2)(y/h)^{n+1}] \tag{1}$$

where $n = 0$ represents a planar flow, and $n = 1$ an axisymmetric flow. Taylor compared Eq. (1) with his own experimental data and found that an inviscid system can also satisfy the no-slip condition of the full Navier–Stokes equations. Experimental investigations[3–5] have revealed that a laminar velocity profile similar to that given by Eq. (1) persists in the mean flow, even if the flow is highly turbulent over the duct cross section. However, the transition of the mean-velocity profile has been observed in experimental investigations.[6–10] Tsai and Liou[10] studied the flow induced by nonuniform in-

Received July 13, 1994; revision received Dec. 28, 1994; accepted for publication Jan. 17, 1995.

*Professor, Department of Power Mechanical Engineering.
†Graduate Student, Department of Power Mechanical Engineering.

jection. Recently, Balakrishnan et al.[11] derived a single integral equation to study the flow in a porous duct and reviewed the issue of the mean-flow transition.

A number of papers have described numerical simulations relevant to the present work. Bankston and Smith[12] solved the laminar Navier–Stokes equations by using a finite difference method. Their results indicated that Eq. (1) becomes valid within a few radii of the closed forward end of the duct. Sviridenkov and Yagodkin[13] assumed the flow to be incompressible and solved the time-averaged Navier–Stokes equations using either a low Reynolds number k-ε or k-ω turbulence model. Their results indicated that the two turbulence models gave qualitatively and quantitatively different predictions. The low Reynolds number k-ω turbulence model proved satisfactory in the pretransition region of mean flow; however, it overpredicted turbulence levels by about 200% in the post-transition region. Although the low Reynolds number k-ε turbulence model proved more satisfactory in the region downstream from the turbulent mean-flow transition point, discrepancies were observed in the pretransition region. Sviridenkov and Yagodkin indicated that the use of both turbulence models may be needed to provide adequate agreement with flow characteristics throughout the duct length. Beddini[14] employed a full Reynolds stress turbulence model to analyze the flows in porous channels. Calculations of turbulence intensity performed by Beddini overpredicted the experimental data of Yamada et al.[4] by about 200%. To attain reasonable agreement with the experimental data of Dunlap et al.,[5] Beddini's calculations[15] had to account for the surface-generated pseudoturbulence in prescribing the boundary conditions. The calculated results were found to be sensitive to the level of pseudoturbulence. Sabnis et al.[16] applied a low Reynolds number k-ε turbulence model to predict the flowfield measured by Dunlap et al.[7] The computed results showed good agreement with the experimental data for the axial mean-velocity profiles, whereas the turbulence level predicted was approximately twice that measured experimentally. In order to calculate the flowfield measured by Traineau et al.,[8] Sabnis et al.[17] had to modify the "low Reynolds number" terms in the k-ε turbulence model and incorporate modified boundary conditions to achieve more accurate simulation. The computed results appeared to predict the turbulence level more closely (the experimental data[8] were overpredicted by about 40% on average throughout the flowfield); however, they predicted a larger move toward the porous wall near the initial shift of the turbulence intensity peak. The above survey of numerical simulations[13–17] is summarized in Table 1, which shows that the turbulence models and turbulence boundary conditions at porous walls varied with the cases considered.

As for other numerical simulations incorporating the wall-function method in flows with wall injection, Elands[18] and Vos[19] used the k-ε turbulence model with wall functions to investigate steady flows in a solid-fuel combustion chamber. The results calculated by Vos showed that the wall-function method worked satisfactorily only for relatively small wall-injection velocities ($v_w \leq 0.05$ m/s), and that the injection velocities used by Elands were within the limits of 0.1 m/s. However, the wall-injection velocities chosen in the experiments on uniform injection[4,5,8,9] were in the range of 1.2–3.1 m/s, and the wall-injection profile in the experiment on non-uniform injection[10] was approximately exponential with a velocity range of $v_w = 0$–7.9 m/s. A unique feature of the flowfield in an SRM is that the head end of the channel is closed and the flow is induced solely by wall mass addition. Therefore, whether the wall function, which is based on the flow in the fully turbulent region, can be applied to the flowfield in an SRM remains an open question.

Our review of these previous investigations[13–17] indicates that existing turbulence models greatly overpredict turbulence levels and are not very successful in predicting the transverse location of the turbulence intensity peak. Furthermore, there is often little justification for the stipulation of the turbulence boundary conditions at the porous walls used in the turbulence models[13–17] because of the difficulty in measuring the flow characteristics near the porous wall. The method used in the present study is to solve the Navier–Stokes equations directly using a modified Godunov's scheme without subgrid-scale (SGS) turbulence models; consequently, the complexity of empirical turbulence models and the limit on the wall-injection velocity associated with a wall function can be avoided. In addition, turbulence parameters such as k, ω, ε, and ι, embedded in the turbulence models, do not need to be specified at porous walls. Liou et al.[20] first used both laser Doppler velocimetry (LDV) measurements and this numerical method to investigate the flowfield induced by nonuniform lateral injection. The computed mean velocity and turbulence intensity were in good agreement with the measured data. Three distinct flow regimes characterizing the flow development in this nonuniform injection-induced flow were recognized both experimentally and computationally. Liou et al.[21] have recently demonstrated the applicability of this numerical method to the study of turbulent nonreacting and reacting flow in a coaxial sudden-expansion solid-fuel combustion chamber. The present work extends the calculation to the flows in a nozzleless SRM and assesses the numerical algorithm by comparing calculated results with existing experimental data.[8] The validity of the "law of the wall" along the porous duct walls encountered in an SRM is also addressed.

Table 1 Summary of existing numerical simulations for injection-driven flows

References	Theoretical methods	Boundary conditions of turbulence models at porous wall	Results
13	Low Re k-ω and k-ε turbulence model	$k = 0$, $\omega = \frac{1}{2}\frac{\partial^2 k}{\partial y^2}$, $\varepsilon = \nu\frac{\partial^2 k}{\partial y^2}$	1. In pretransition: k-ω predict well 2. In post-transition: k-ω overpredict I by about 200%; k-ε overpredict I by about 30%
14	Full Re stress turbulence model	All Reynolds stresses are zero	Overpredict I of Yamada[4] by about 200%
15	Full Re stress turbulence model	$\overline{u'u'} = \overline{u'v'} = \overline{w'w'} = 0$ $0.035 \leq \sigma_v \leq 0.078$	1. $\sigma_v = 0.078$: overpredict I of Dunlap[5] by about 100% 2. $\sigma_v = 0.035$: predict well
16	Low Re k-ε turbulence model	$k = \varepsilon = 0$	Overpredict k, Reynolds stress of Dunlap[9] by about 100%
17	Modified low Re k-ε turbulence model	$k_w = k_\phi[1 - \exp(-v_w^+/B^+)]$ $\iota_w = \iota_\phi[1 - \exp(-v_w^+/B^+)]$	Overpredict I of Traineau[8] by about 40%

Governing Equations and Numerical Algorithm

A major objective of this article is to study the transition process occurring in an injection-driven porous duct flow. It is possible that the transition corresponds to the onset of instability of the boundary layer for asymmetric disturbances and is a result of the very high relative turbulence intensity of the injected fluid at the wall, as described in the work of Balakrishnan et al.[11] They found that the compressibility effects flatten radial profiles of axial velocity (i.e., transition) when a two-dimensional theoretical analysis is used. Sabnis et al.[17] performed a two-dimensional computation and also predicted the transition process. In addition, Traineau et al.[8] claimed that the present simulated flow is a cold flow of a two-dimensional nozzleless SRM. Tsai and Liou[10] demonstrated that two dimensionality existed in their measurement of flow induced by nonuniform lateral injection. This valuable information suggests that the present simulations can be formulated in a two-dimensional form.

Governing Equations

Figure 1 presents a schematic drawing of the computational domain, which consists of a closed-end porous duct and an impermeable-walled diverging expansion area, where y is the transverse distance from the injecting wall. Assuming that there are no external heat additions and body forces, the compressible Navier–Stokes equations in two-dimensional Cartesian coordinates can be written as

$$\frac{\partial \boldsymbol{Q}}{\partial t} + \frac{\partial \boldsymbol{F}}{\partial x} + \frac{\partial \boldsymbol{G}}{\partial y} = 0 \tag{2}$$

where $\boldsymbol{Q}$, $\boldsymbol{F}$, and $\boldsymbol{G}$ are vectors given by

$$\boldsymbol{Q} = \begin{bmatrix} \rho \\ \rho u \\ \rho v \\ e \end{bmatrix}, \qquad \boldsymbol{F} = \begin{bmatrix} \rho u \\ \rho u^2 + \tau_{xx} \\ \rho uv + \tau_{yx} \\ (e + \tau_{xx})u + \tau_{yx}v - \kappa \dfrac{\partial T}{\partial x} \end{bmatrix}$$

$$\boldsymbol{G} = \begin{bmatrix} \rho v \\ \rho uv + \tau_{xy} \\ \rho v^2 + \tau_{yy} \\ (e + \tau_{yy})v + \tau_{xy}u - \kappa \dfrac{\partial T}{\partial y} \end{bmatrix}$$

and τ is the shear stress, which can be defined as

$$\tau_{xx} = p - \lambda\left(\frac{\partial u}{\partial x} + \frac{\partial v}{\partial y}\right) - 2\mu \frac{\partial u}{\partial x}$$

$$\tau_{yy} = p - \lambda\left(\frac{\partial u}{\partial x} + \frac{\partial v}{\partial y}\right) - 2\mu \frac{\partial v}{\partial y}$$

$$\tau_{xy} = \tau_{yx} = -\mu\left(\frac{\partial u}{\partial y} + \frac{\partial v}{\partial x}\right)$$

The equations, written in the form of conservation laws, represent the conservation of mass, momentum, and total energy of fluid motion, respectively.

Numerical Algorithm

The code uses the finite volume technique, which discretizes the integral formulation of conservation laws in a physical space composed of a set of small control volumes. Because conservation laws are enforced over each cell, the physical quantities of mass, momentum, and energy will remain conserved. Vector $\boldsymbol{Q}$ in Eq. (2), representing conservation variables, was calculated at the center of each computational cell, and flux vectors $\boldsymbol{F}$ and $\boldsymbol{G}$ in Eq. (2) were calculated at the cell edges using Godunov's scheme. The basic idea behind Godunov's scheme is to use the exact solution of gasdynamic equations with piecewise initial states to construct the finite difference schemes. Godunov used characteristic information so that the Riemann problem could be solved forward in time, and then used the solution of the Riemann problem to calculate the numerical flux at the cell edges. The major disadvantage of Godunov's original scheme is the first-order spatial accuracy, which results in a relatively poor resolution of flow structure. In order to improve the order of spatial accuracy of Godunov's original scheme, the piecewise initial states to the left and right of the cell edges were obtained by a second-order extrapolation in the present work. In addition, a limiting technique was applied to achieve numerical stability. A detailed derivation of the modified Godunov's scheme is presented in the work of Liou et al.[22]

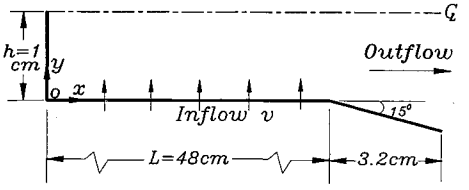

Fig. 1 Schematic diagram of computational domain for test case.

Boundary and Initial Conditions

The primitive variables (ρ, u, v, p) must be specified at the boundaries because they are involved in the flux vectors. At the head end of the channel, no-slip conditions are used along with an adiabatic wall and zero normal pressure gradient. At the centerline of the channel, the symmetry conditions are applied for all primitive variables. Characteristic-based boundary conditions are enforced on the inflow and outflow boundaries in compressible flows. At the inflow, both mass flux and energy flux are kept constant with $u = 0$ specified since there are three incoming characteristics and one outgoing characteristic for the subsonic inlet velocity. At the expander exit, there are four outgoing characteristics for the supersonic outlet velocity, and the outflow boundary conditions need not be specified. Specification of the initial conditions is based on the experimental measurements of Traineau et al.[8]

Grid Independence

The numerical results should be independent of the grid size; a grid-independence study was performed by checking the axial mean-velocity and turbulence intensity. Five sets of grids, 258 × 22, 386 × 32, 514 × 42, 642 × 52, and 770 × 62 ($x \times y$), were examined, and grid independence was attained for grid sizes of 642 × 52 and 770 × 62. The average deviations of the axial mean velocity $\bar{u}$ and turbulence intensity I throughout the flowfield calculated from these two grid systems were only 0.1 and 0.75%, respectively; the local maximum deviations observed near the channel head-end (x = 0.08, y = 0.01 cm) were only 0.25 and 1.6% for $\bar{u}$ and I, respectively. Therefore, the results presented below are based on the 642 × 52 grid system. The calculations were performed with a system of nonuniform grids clustered at the porous wall and the beginning of the expander. The smallest axial resolution was 3×10^{-3} mm at the beginning of the expander, and the smallest transverse resolution was 10^{-3} mm near the porous wall based on the 642 × 52 grid. This near-wall grid resolution provides viscous sublayer resolution, as will be shown later. The Courant number fixed at 0.6 to guarantee numerical stability and to advance the code in time properly results in a temporal resolved scale of 1.7×10^{-9} s. Although the

present numerical method solves the Navier–Stokes equations directly without SGS turbulence models, numerical dissipation was considered as a crude SGS model in many other investigations.[23–25] In fact, the numerical dissipation here is proportional to Δ^2 (Δ being the grid resolution), which is very similar to the normal SGS model of dissipative nature.[26]

As with experiments, statistical data including mean velocity and turbulence intensity can be obtained by taking a time average from the time-dependent solution over an appropriate period of time. Several sets of time intervals (Δt), e.g., 4.2–6.3, 4.2–8.4, 8.4–12.6, and 8.4–14.7 ms, were examined in this study, and the average deviations of mean velocity and turbulence intensity throughout the flowfield calculated from Δt = 8.4–12.6 and 8.4–14.7 ms were found to be less than 0.5%. Therefore, the time-averaged results extracted from the fluctuating field over the time interval ($8.4 \leq t \leq 12.6$ ms) attained the asymptotic converged solutions. The calculations were carried out on a DEC 3000 model 600 workstation and a complete run for the statistical data required about 280 hours of CPU time.

Results and Discussion

Mean Flow

The computed results depicted in Figs. 2 and 3 are variations of normalized static pressure and axial mean velocity vs axial distance. Experimental data[8] are also included for comparison. Good agreement is found between computed results and experimental data within the axial distance of x/L = 0.5, and some slight deviations are found in the downstream region. Figure 4 compares the computed axial mean-velocity profiles at various axial locations with the experimental data of Traineau et al.[8] and the calculations of Sabnis et al.[17] The normalized axial mean-velocity profiles of the experimental data exhibit a similar distribution pattern for $x/h \leq 19$, and the analaytic solution of laminar theory $\{\bar{u}/\bar{u}_c = \sin[(\pi/2)(y/h)]\}$ agrees well with the experimental data in this region. After x/h = 19, the experimental profiles diverge from the laminar theory solutions and continue to fill out toward the aft end of the channel. This behavior shows the transition from the laminar to the turbulent mean-velocity profiles occurring in the experiment; clearly, the laminar theory cannot be applied downstream of the transition. However, the turbulent effects appear to be smoothed by the compressibility effects, as evidenced by comparing the one-seventh power-law profile with the experimental data in the close vicinity of the throat where the axial mean velocity is supersonic over half of the channel (e.g., M_c = 1.13 at x/h = 47).[8] Both calculations predict a tendency similar to that observed in the experiment in the mean-flow velocity transition and compressibility effects, whereas the profiles of Sabnis et al.[17] appear to be "fuller" than the experimental data. Note that the fuller velocity profiles may overpredict the turbulence gradient.

To verify that the present numerical method captures the expansive wave structures in the diverging expansion region, in Fig. 5 we compare the calculated pressure contours near this region with the experimental data. The calculated results predict that large pressure gradients will occur near the porous wall of the injection duct and along the centerline of the expansion area. These trends are also found in the experimental data. Furthermore, good agreement between calculations and measurements in the supersonic region ($x/L \geq 1$) indicates that the present method has resolved the wave structures in the diverging expansion region.

Mean-Flow Transition

Because the normalized axial mean-velocity profiles shown in Fig. 4 cannot provide a precise axial location for the mean-

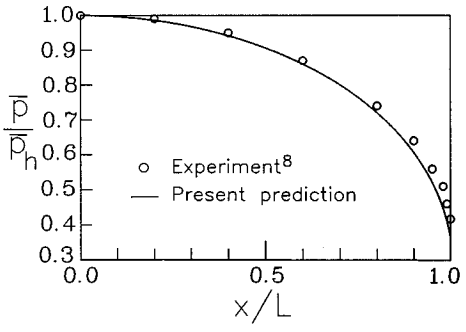

Fig. 2 Variation of normalized mean static pressure with axial distance.

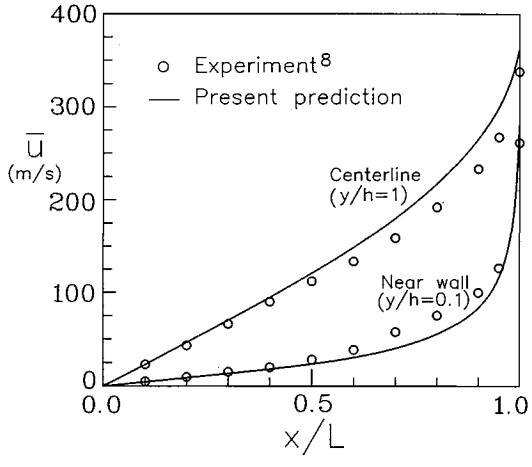

Fig. 3 Variation of axial mean velocity with axial distance.

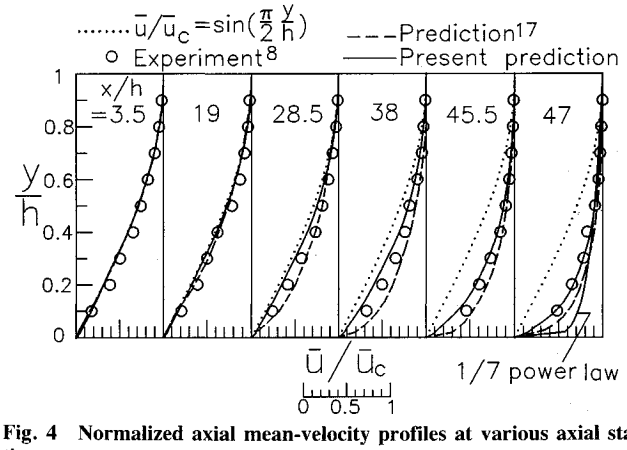

Fig. 4 Normalized axial mean-velocity profiles at various axial stations.

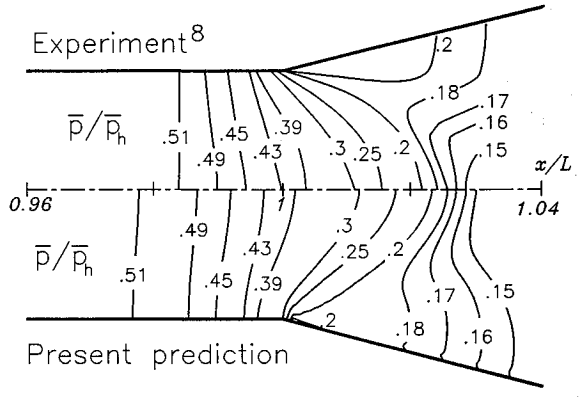

Fig. 5 Normalized mean static pressure contours near diverging expansion region.

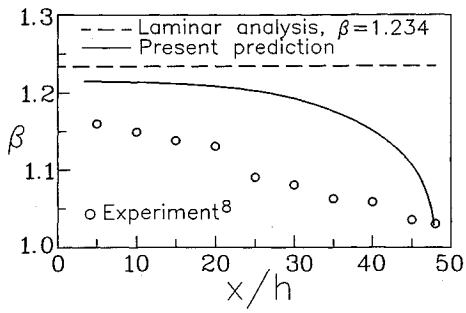

Fig. 6 Variation of momentum flux coefficient with axial distance.

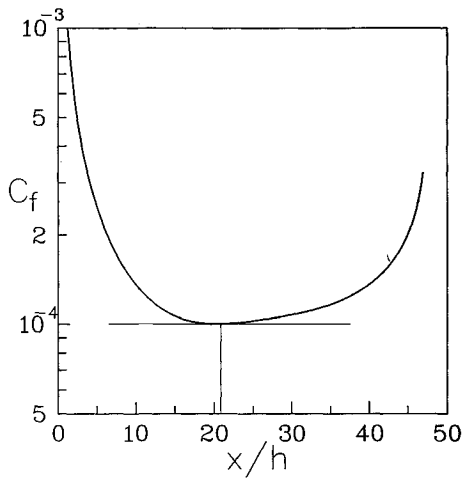

Fig. 7 Axial variation of skin friction coefficient.

flow transition, an alternative way to identify where the transition occurs is to examine the axial variation of the momentum flux coefficient β, as proposed by Huesmann and Eckert.[7] Figure 6 compares the present computed axial variations of β with the experimental data.[8] It is worth noting that the experimental value of β is 1.16 at the head-end instead of 1.234 as predicted by the laminar theory, because of the high pseudoturbulence levels at the porous wall and the rather large scattering of measured data, and that it shows a faster variation between $x/h = 20$ and $x/h = 30$. The variation of β is an indication of a changing axial mean-velocity profile; it is therefore reasonable to assimilate the fast variation at $x/h = 20$ to the onset of the mean-flow transition. In contrast, the present calculations show a smoother variation of β from the head-end to exit. This gradual variation in the computed β may be a distinctive feature of numerical simulations, since the spatial resolution of calculations is finer than that in experiments. However, it also reveals that the axial mean-velocity profile actually undergoes a change along the channel. The degree of decrease in β associated with the transition of the mean-velocity profile is yet to be determined. A more definitive way to locate the axial location of the mean-flow transition is to examine the axial variation of the skin friction coefficient C_f, as is usual in fluid mechanics. Figure 7 shows the axial variation of the present computed C_f, and indicates that the mean-flow transition occurs at about the same axial location as in experiments ($x/h = 20$). The mean-flow transition occurs when C_f begins to increase.

Other evidence of the mean-flow transition comes from the theoretical curve calculated by Beddini[15] that depicts the variation of the centerline axial Reynolds number Re_c with the injection Reynolds number Re_w. It is interesting to compare the Re_c at which the measured mean-velocity profile transition occurs ($Re_c = 2.5 \times 10^5$ at $x/h = 20$) with both Beddini's theoretical curve and the present predictions. Such a comparison is depicted in Fig. 8, which also includes the linear-

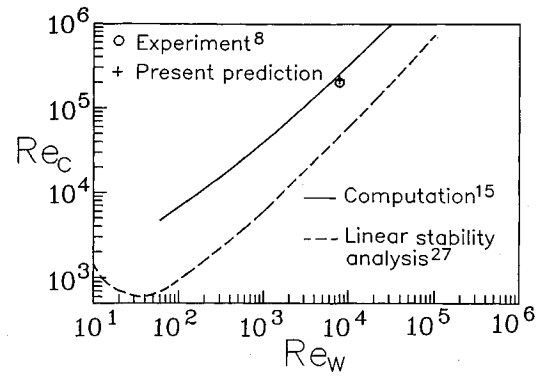

Fig. 8 Variation of Re_c with Re_w for axial mean-velocity transition.

stability curve of Varapaev and Yagodkin.[27] The computed Re_c, in close agreement with the experimental data, further shows that the present numerical method of predicting the axial location of the transition from the laminar to turbulent mean flow is reasonably accurate.

Turbulence-Intensity Profiles

Further comparison of the present predictions, the computations of Sabnis et al.[17] and the measurements of Traineau et al.[8] are presented in Fig. 9 in terms of turbulence intensity distributions for several axial locations. From the experimental data, the peak value of the turbulence intensity I_p appears midway between the channel centerline and porous surface for $x/h \leq 20$. Beyond $x/h = 20$, the turbulence intensity increases rapidly, and I_p shifts toward the porous wall as the streamwise coordinate increases. Physically, the maximum turbulence intensity occurring adjacent to the propellant surface can enhance the heat transfer rate and mixing rate of decomposition gases so that the burning rate is augmented and erosive burning is initiated. This implies that there is an intimate relation between the shift in I_p and the ballistics of an SRM, since the ballistics is affected by erosive burning. An examination of Fig. 9 indicates that previous calculations[17] predict a larger move toward the porous wall near the initial I_p shift ($x/h = 24$) and overpredict the measured I_p by about 60%. In terms of the turbulence gradient I_p/y_p, which is closely related to the erosive burning,[4] the overprediction will be 130% of the measured value. The present computed I_p/y_p at $x/h = 24$ agrees with the experimental data, but the present calculations miss the location of I_p at $x/h = 30$, resulting in a larger deviation in I_p/y_p (31% underprediction) compared with the previous calculations (28.9% overprediction). Nevertheless, both calculations capture the features of the measured turbulence-intensity variation reasonably well.

Law of the Wall

As addressed in the foregoing survey of the literature, attempts to carry out calculations with the wall-function method at high injection velocities have been unsuccessful,[18,19] and numerical simulations relevant to the flowfield in an SRM have not employed this method.[13-17] Therefore, it is interesting to consider what physical insights we have regarding the effects of wall injection on the near-wall velocity profiles for injection through a porous surface with crossflow and the "law of the wall" throughout the flowfield in an SRM. In the measured results of Schetz and Nerney[28] for injection through a sintered metal porous surface with crossflow, the logarithmic portion of the wall law was unaffected by injection, and only shifted downward from the smooth, solid-wall results by an amount $\Delta u^+ = 3.5$ due to the relatively low blowing rates. However, the experimental data of Moffat and Kays[29] for the fully turbulent flat-plate flow with blowing showed that as the blowing rate increased, the velocity profiles rose dramatically from the logarithmic portion. These results imply that the

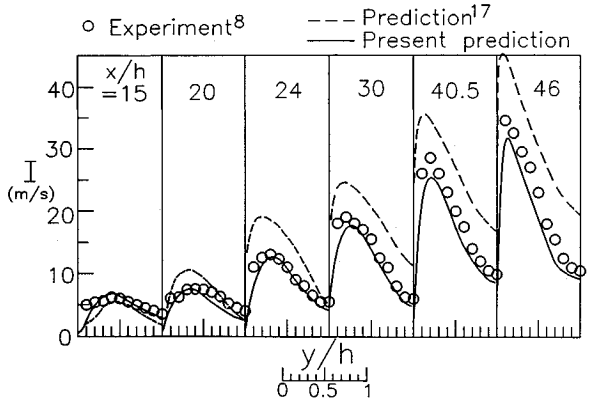

Fig. 9 Turbulence intensity distributions at various axial stations.

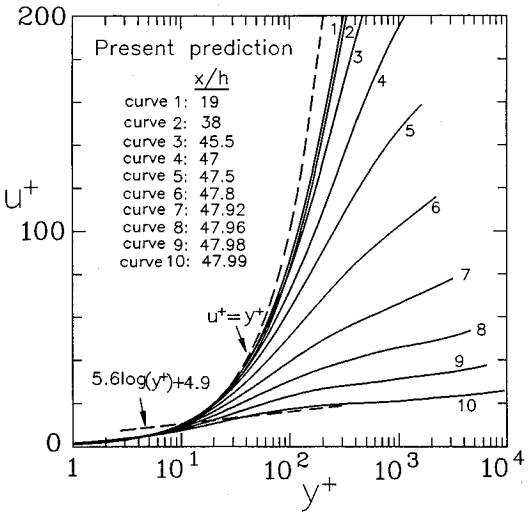

Fig. 10 Axial mean-velocity profiles normalized by wall-shear velocity at various axial stations.

logarithmic law of a solid surface cannot be applied to a porous surface with a high blowing rate. Richardson et al.[30] employed a procedure similar to that of Patankar and Spalding,[31] and used the data of Moffat and Kays[29] to develop a modified logarithmic law that included the effects of wall-mass addition.

For the present simulations of injection-driven flows in a nozzleless SRM,[8] the computed axial mean-velocity profiles normalized by wall-shear velocity at various streamwise locations are shown in Fig. 10. The dashed lines represent the laminar wall law for the viscous sublayer ($u^+ = y^+$) and the logarithmic law ($u^+ = 5.6 \log y^+ + 4.9$) of a solid surface. The near-wall grid resolution in terms of y^+ changes from 0.05 at $x/h = 0$ to 1.03 at $x/h = 48$ along the channel, which provides a viscous sublayer resolution ($y^+ \leq 5$) throughout the flowfield in the porous wall duct. The computed normalized mean-velocity profiles satisfy the laminar viscous sublayer wall law for $y^+ \leq 5$ at all streamwise locations; for $y^+ > 5$, they change gradually from the laminar to the fully turbulent profile (curve 10) along the porous channel and cannot be collapsed into a unique universal wall law throughout the flowfield. This observation indicates that the wall-function method cannot be applied to an SRM flowfield because this method assumes that the streamwise mean-velocity component follows the logarithmic law at a point outside the viscous sublayer (usually the first grid node off the wall boundary) throughout the flowfield considered. In order to render the wall-function method unnecessary, the near-wall grid resolution in the transverse direction must provide a viscous sublayer resolution, as demonstrated by the computed normalized mean velocities for $y^+ \leq 5$.

Concluding Remarks

The injection-driven flows in a two-dimensional nozzleless SRM have been simulated numerically by solving the time-dependent compressible Navier–Stokes equations directly without subgrid-scale turbulence models for the first time. A comparison of the present numerical results with previous calculations incorporating turbulence models demonstrates that the present method represents a significant improvement in predicting the mean-velocity profile and turbulence level for injection-driven flows. In addition, the present numerical simulations predict the axial location of the transition from the laminar to the turbulent mean flow and the transverse location of the turbulence intensity peak reasonably well. The compressibility effects and wave structures at the expander in the nozzleless SRM have also been modeled by the present method.

The present calculations have demonstrated that the mean-velocity profiles in the inner coordinate away from the viscous sublayer vary along the porous channel and cannot be correlated into a single universal wall law throughout the flowfield in a nozzleless solid-rocket motor. This fact provides a rationale to explain why the wall-function method cannot be applied to injection-driven flows in an SRM.

Acknowledgment

This research was supported by the National Science Council of the Republic of China under Contract CS81-0210-D007-1003.

References

[1]Taylor, G. I., "Fluid Flow in Regions Bounded by Porous Surfaces," *Proceedings of the Royal Society of London*, Series 234A, Vol. 1199, 1956, pp. 456–475.

[2]Culick, F. E. C., "Rotational Axisymmetric Mean Flow and Damping of Acoustic Waves in Solid Propellant Rocket Motors," *AIAA Journal*, Vol. 4, No. 8, 1966, pp. 1462–1464.

[3]Wageman, W. E., and Guervara, F. A., "Fluid Flow Through a Porous Channel," *Physics of Fluids*, Vol. 3, No. 6, 1960, pp. 878–881.

[4]Yamada, K., Goto, M., and Ishikawa, N., "Simulative Study on the Erosive Burning of Solid Rocket Motors," *AIAA Journal*, Vol. 14, No. 9, 1976, pp. 1170–1176.

[5]Dunlap, R., Willoughby, P. G., and Hermsen, R. W., "Flowfield in the Combustion Chamber of a Solid Propellant Rocket Motor," *AIAA Journal*, Vol. 12, No. 12, 1974, pp. 1440–1442.

[6]Olson, R. M., and Eckert, E. R. G., "Experimental Studies of Turbulent Flow in a Porous Circular Tube with Uniform Fluid Injection Through the Tube Wall," *Journal of Applied Mechanics*, Vol. 33, No. 4, 1966, pp. 7–17.

[7]Huesmann, K., and Eckert, E. R. G., "Studies of the Laminar Flow and the Transition to Turbulence in Porous Tubes with Uniform Injection Through the Tube Wall," *Warme- und Stoffubertragung*, Bd. 1, 5.2, 1968, pp. 2–9.

[8]Traineau, J. C., Hervat, P., and Kuentzmann, P., "Cold-Flow Simulation of a Two-Dimensional Nozzleless Solid-Rocket Motor," AIAA Paper 86-1447, June 1986.

[9]Dunlap, R., Blackner, A. M., Waugh, R. C., Brown, R. S., and Willoughby, P. G., "Internal Flow Field Studies in a Simulated Cylindrical Port Rocket Chamber," *Journal of Propulsion and Power*, Vol. 6, No. 6, 1990, pp. 690–705.

[10]Tsai, M. K., and Liou, T. M., "Study of Flow Induced by Non-uniform Lateral Injection," *Journal of Propulsion and Power*, Vol. 7, No. 5, 1991, pp. 668–678.

[11]Balakrishnan, G., Liñán, A., and Williams, F. A., "Rotational Inviscid Flow in Laterally Burning Solid-Propellant Rocket Motors," *Journal of Propulsion and Power*, Vol. 8, No. 6, 1992, pp. 1167–1176.

[12]Bankston, C. A., and Smith, H. J., "Vapor Flow in Cylindrical Heat Pipes," *Journal of Heat Transfer*, Vol. 95, No. 8, 1973, pp. 371–376.

[13]Sviridenkov, A. A., and Yagodkin, V. I., "Flows in the Initial Sections of Channels with Permeable Walls," *Fluid Dynamics*, Vol. 11, No. 5, 1976, pp. 43–48.

[14]Beddini, R. A., "Aerothermochemical Analysis of Erosive Burning in a Laboratory Solid-Rocket Motor," *AIAA Journal*, Vol. 18,

No. 11, 1980, pp. 1346–1353.

[15]Beddini, R. A., "Injection-Induced Flows in Porous-Walled Ducts," *AIAA Journal*, Vol. 24, No. 11, 1986, pp. 1766–1773.

[16]Sabnis, J. S., Gibeling, H. J., and McDonald, H., "Navier-Stokes Analysis of Solid Propellant Rocket Motor Internal Flows," *Journal of Propulsion and Power*, Vol. 5, No. 6, 1989, pp. 657–664.

[17]Sabnis, J. S., Madabhushi, R. K., Gibeling, H. J., and McDonald, H., "On the Use of k-ε Turbulence Model for Computation of Solid Rocket Internal Flows," AIAA Paper 89-2558, July 1989.

[18]Elands, P. J. M., "The Prediction of the Flow and Combustion in a Solid Fuel Combustion Chamber by Means of Two Combustion Models Based on the Diffusion Flame Concept," AIAA Paper 87-1702, June 1987.

[19]Vos, J. B., "Calculating Turbulent Reacting Flows Using Finite Chemical Kinetics," *AIAA Journal*, Vol. 25, No. 10, 1987, pp. 1365–1372.

[20]Liou, T. M., Lien, W. Y., and Tsai, G. S., "Experimental and Computational Studies of Fluid Flow in a Two-Dimensional Porous-Walled Channel," *Ninth Symposium on Turbulent Shear Flows* (Kyoto, Japan), Springer–Verlag, Berlin, 1993, pp. 5-4-1–5-4-6.

[21]Liou, T. M., Lien, W. Y., and Hwang, P. W., "Large-Eddy Simulations of Turbulent Reacting Flows in a Chamber with Gaseous Ethylene Injecting Through the Porous Wall," *Combustion and Flame*, Vol. 99, Nos. 3/4, 1994, pp. 591–600.

[22]Liou, T. M., Lien, W. Y., and Hwang, P. W., "A Modified Godunov's Scheme for Shock Tube Flows and Turbulent Combustion Flows," *4th National Conference on Combustion Science and Technology*, The Combustion Inst. of ROC, Hsinchu, Taiwan, ROC, 1994, pp. 242–247.

[23]Jou, W. H., and Riley, J. J., "Progress in Direct Numerical Simulations of Turbulent Reacting Flows," *AIAA Journal*, Vol. 27, No. 11, 1989, pp. 1543–1556.

[24]Kailasanath, K., Gardner, J. H., Boris, J. P., and Oran, E. S., "Numerical Simulations of Acoustic-Vortex Interactions in a Central-Dump Ramjet Combustor," *Journal of Propulsion and Power*, Vol. 3, No. 6, 1987, pp. 525–533.

[25]Kailasanath, K., Gardner, J. H., Boris, J. P., and Oran, E. S., "Acoustic-Vortex Interactions and Low-Frequency Oscillations in Axisymmetric Combustors," *Journal of Propulsion and Power*, Vol. 5, No. 2, 1989, pp. 165–171.

[26]Smagorinsky, J., "General Circulation Experiments with the Primitive Equations," *Monthly Weather Review*, Vol. 91, No. 3, 1963, pp. 99–164.

[27]Varapaev, V. N., and Yagodkin, V. I., "Flow Stability in a Channel with Porous Walls," *Fluid Dynamics*, Vol. 4, No. 5, 1969, pp. 91–95.

[28]Schetz, J. A., and Nerney, B., "Turbulent Boundary Layer with Injection and Surface Roughness," *AIAA Journal*, Vol. 15, No. 9, 1977, pp. 1288–1294.

[29]Moffat, R. J., and Kays, W. M., "A Review of Turbulent Boundary Layer Heat Transfer Research at Stanford, 1958–1983," *Advances in Heat Transfer*, Vol. 16, 1984, pp. 241–365.

[30]Richardson, J., De Groot, W. A., Jagoda, J. I., Walterick, R. E., Hubbartt, J. E., and Strahle, W. C., "Solid Fuel Ramjet Simulator Results: Experiment and Analysis in Cold Flow," *Journal of Propulsion and Power*, Vol. 1, No. 6, 1985, pp. 488–493.

[31]Patankar, S. V., and Spalding, D. B., *Heat and Mass Transfer in Boundary Layers*, 2nd ed., Intertext Books, London, 1970.